CRYSTAL GROWTH & DESIGN

Article

Cite This: Cryst. Growth Des. 2020, 20, 362−369

pubs.acs.org/crystal

Lanthanide-Incorporated Borotungstates Including Keggin-type $[BW_{11}O_{39}]^{9-}$ Fragments and Their Luminescence Properties

Jun Jiang,[†] Jiaru Duan,[†] Jiancai Liu,[†] Lijuan Chen,*[,†] and Junwei Zhao*[,†,‡]

[†]Henan Key Laboratory of Polyoxometalate Chemistry, College of Chemistry and Chemical Engineering, Henan University, Kaifeng, Henan 475004, People's Republic of China

[‡]State Key Laboratory of Structural Chemistry, Fujian Institute of Research on the Structure of Matter, Chinese Academy of Sciences, Fuzhou, Fujian 350002, People's Republic of China

Supporting Information

ABSTRACT: Three kinds of lanthanide (Ln)-substituted borotungstates including $[BW_{11}O_{39}]^{9-}$ segments $KH_2[Ce(H_2O)_8][(\alpha\text{-}BW_{11}O_{39})Ce(H_2O)_3]\cdot 14H_2O$ (**1**), $K_2Na_2H_2[(\alpha\text{-}BW_{11}O_{39})Pr(H_2O)_3]\cdot 15H_2O$ (**2**), and $Na_3K_8H[W_5O_{18}]Ln[\alpha\text{-}BW_{11}O_{39}]\cdot 22H_2O$ [Ln = Eu^{3+} (**3**), Dy^{3+} (**4**), Ho^{3+} (**5**), Yb^{3+} (**6**)] were manufactured. Compound **1** adopts a one-dimensional (1-D) zigzag chain by fusing adjacent $[Ce(H_2O)_8][(\alpha\text{-}BW_{11}O_{39})Ce(H_2O)_3]^{3-}$ polyoxoanions in the help of Ce^{3+} bridging. It is worth noting that adjoining chains can be interacted with each other by K^+ cations and give birth to a fascinating two-dimensional sheet. In contrast, the polyoxoanion of **2** is assembled from a mono-Pr^{III} embedded $[(\alpha\text{-}BW_{11}O_{39})Pr(H_2O)_3]^{6-}$ unit, which also propagates an analogical 1-D chain like **1** without hanging $[Ln(H_2O)_8]^{3+}$ cations. Compounds **3**−**6** display a typical mixed-POM dimeric assembly composed of monovacant Keggin $[\alpha\text{-}BW_{11}O_{39})]^{9-}$ and monovacant Lindqvist $[W_5O_{18}]^{6-}$ segments concatenated by an Ln cation. Luminescence performances of **3**−**5** were systematically probed at ambient temperature, exhibiting the featured emissions from f−f transitions of Ln ions. Meanwhile, energy transfer from borotungstate fragment to Ho^{3+} ion was observed in the emission process of **5**.

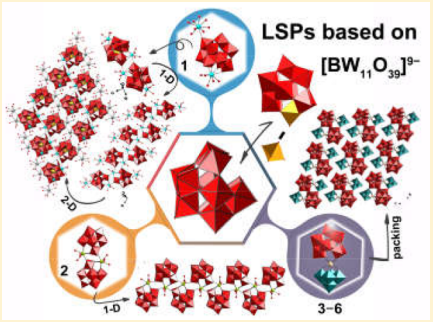

INTRODUCTION

Polyoxometalates (POMs) have intensively appealed to increasing research enthusiasm in recent years, not only owing to their unrivalled structural diversities and charming topological aesthetics but also because of their immense applications in catalysis, medicine, electronics, magnetism, optics, and so forth.[1−7] It is noteworthy that POMs can function as multidentate ligands to incorporate diverse transition-metal (TM) or lanthanide (Ln) cations into multifarious POM building units, stimulated by their intrinsic properties of high negative charge density and O-enriched surfaces.[8] In this regard, lacunary POMs have attracted high interest in the field of synthesis, which are more prone to coalesce with oxophilic metal cations than plenary POMs due to the chelating coordination of terminal oxygen atoms from the defect sites of POMs, and then those captured metal cations can act as additional extension points to fuse other segments together generating ingenious TM-incorporated POMs (TMSPs) or Ln-incorporated POMs (LnSPs).[9−13]

Borotungstates (BTs), as an imperative subfamily of POM chemistry with noteworthy diversity in terms of exclusive structures, compositions, and properties, have evoked great interest and also have made some progress since $K_5[BW_{12}O_{40}]$ was first synthesized by Rocchiccioli-Deltcheff et al. in 1983,[14,15] whereas what deserves attention is that reports on BTs are much less than those containing other heteroatoms from main groups IV, V, and VI. A valid strategy of enriching structural diversity of BTs is to introduce oxophilic TM/Ln ions into the system, acquiring a number of peculiar TMSPs/LnSPs based on BT fragments of $[BW_{11}O_{39}]^{9-}$ ($\{BW_{11}\}$), $[BW_{12}O_{40}]^{5-}$ ($\{BW_{12}\}$), or $[BW_{13}O_{46}]^{11-}$ ($\{BW_{13}\}$). After years of tough work, a wealth of examples of TM-containing BTs have been reported. When it comes to TMSPs based on $\{BW_{11}\}$ fragments, it is noteworthy that Ritchie et al. reported the first photochromic BT-based diarylethene coordination complex $[(C_{25}H_{16}N_2F_6S_2)(BW_{11}O_{39}Co)_2]^{12-}$ in 2018, which was made by connecting two cobalt(III)-incorporated $[BW_{11}O_{39}Co]^{6-}$ segments with pyridyl-containing diarylethene.[16] Wang and co-workers combined copper−amino acid cations with $\{BW_{12}\}$ units and obtained chiral three-dimensional (3-D) frameworks with helical channels.[17,18] To our knowledge, acidification of $\{BW_{11}\}$ in the presence of tungstate not only can generate $\{BW_{12}\}$ but also can form other derivatives such as $\{BW_{13}\}$ that are derived from Keggin-type undecatungstic anion capped by a μ-oxoditungstic $\{W_2O_{11}\}$ group.[19−21] It was not until 2013 that Reinoso et al. managed to obtain an Fe^{III}-substituted BT derivative $[\{Fe(H_2O)_3\}_2(WO_2)(HBW_{11}O_{39})_2]^{8-}$, which is an unparalleled 2-boro-23-tungstate unit stabilized by Fe^{3+} ions at external positions, delegating the first TM substitution in the

Received: September 30, 2019
Revised: October 31, 2019
Published: November 15, 2019

Downloaded via HENAN UNIV on January 4, 2020 at 07:10:09 (UTC).
See https://pubs.acs.org/sharingguidelines for options on how to legitimately share published articles.

© 2019 American Chemical Society

DOI: 10.1021/acs.cgd.9b01290
Cryst. Growth Des. 2020, 20, 362−369

{BW_{13}} framework.[22] Currently, a lot of TM-containing BTs have been reported by varying BT building units or changing TM species.[23−28] However, related reports on Ln-substituted BTs (LnSBTs) are underdeveloped. In contrast to TM cations, Ln ions possess the following characteristics: (i) high coordination numbers and ample bonding modes may result in different structure types; (ii) in line with the Hard and Soft Acids and Bases theory,[29] Ln ions are oxophilic so that they can swimmingly coordinate to oxygen atoms as connectors or ornaments, which may lead to extended structures; (iii) Ln ions own peculiar luminous properties like long lifetime and narrow emitting bandwidth, playing an indispensable role in the optical field.[30] As a consequence, the synthesis and property exploration of LnSBTs have continued to be a focus of intense research in POM field. Within this field, the research hotspot prevailingly points at taking advantage of monovacant {BW_{11}} precursor as a multidentate chelating ligand to capture Ln ions to construct LnSBTs. Some incunabular reports have emerged with the discovery of 1:1-type complexes $[Ln(BW_{11}O_{39})(H_2O)_3]^{6-}$ (Ln = Sm^{3+}, Eu^{3+}, Tb^{3+}, Er^{3+}) as well as 1:2-type complexes $[Eu(BW_{11}O_{39})_2]^{15-}$.[31,32] Subsequently, an exceptional one-dimensional (1-D) chain $[Ce_2(BW_{11}O_{39})_2(H_2O)_6]^{12-}$ was also triumphantly achieved in 2005.[33] After a relatively long-standing sluggish period, An et al. discovered a class of organic−inorganic hybrid 3-D framework $[(C_6NO_2H_5)Ln(H_2O)_5]_2[(H_2O)_4LnBW_{11}O_{39}H]_2^{4-}$ (Ln = Ce^{3+}, Nd^{3+}, $C_6NO_2H_5$ = pyridine-4-carboxylic acid) in 2010.[34] Besides, a family of quadruple-gly bridging dimeric LnSBTs $[Ln_2(gly)_4(BW_{11}O_{39})_2]^{12-}$ (Ln = Ce^{3+}, Pr^{3+}, Nd^{3+}, Sm^{3+}, Eu^{3+}, Tm^{3+}; gly = glycine) were isolated by our lab in 2016, delegating the first case of inorganic−organic hybrid LnSBTs based on monovacant {BW_{11}} segments, Ln cations, and amino acid linkers.[8] Above sporadic examples reveal that there exists an enormous challenge to design and fabricate neoteric LnSBTs based on lacunary BT segments and Ln ions.

Enlightened by the previous exploration, we performed systematic explorations to discover novel LnSBTs based on lacunary BT segments and Ln ions. Fortunately, three kinds of LnSBT aggregates $KH_2[Ce(H_2O)_8][(\alpha\text{-}BW_{11}O_{39})Ce(H_2O)_3]\cdot 14H_2O$ (**1**), $K_2Na_2H_2[(\alpha\text{-}BW_{11}O_{39})Pr(H_2O)_3]\cdot 15H_2O$ (**2**), and $Na_3K_8H[W_5O_{18}]Ln[\alpha\text{-}BW_{11}O_{39}]\cdot 22H_2O$ [Ln = Eu^{3+} (**3**), Dy^{3+} (**4**), Ho^{3+} (**5**), Yb^{3+} (**6**)] were successfully prepared using an aqueous solution method (Figure 1). In this work, **1** and **2** were synthesized by a stepwise synthesis using $K_8[\alpha\text{-}BW_{11}O_{39}H]\cdot 13H_2O$ as the precursor, and **3**−**6** were harvested via a one-pot self-assembly strategy based on simple commercial materials ($Na_2WO_4\cdot 2H_2O$, H_3BO_3, and $Ln(NO_3)_3\cdot 6H_2O$). The asymmetrical molecular fragment of **1** comprises a mono-Ce^{III}-substituted Keggin $[(\alpha\text{-}BW_{11}O_{39})Ce(H_2O)_3]^{6-}$ moiety supported by a decorated $[Ce(H_2O)_8]^{3+}$ cation on one side, and neighboring molecular units are joined together via W−O−Ce−O−W linkages to generate a 1-D zigzag chainlike alignment. Compound **2** exhibits an analogical 1-D chain arrangement to **1** without decorated $[Pr(H_2O)_8]^{3+}$ cations. Compounds **3**−**6** feature a typical dimeric asymmetrical assembly and consist of an Ln cation connecting a monovacant Keggin {BW_{11}} and a monovacant Lindqvist $[W_5O_{18}]^{6-}$ subunits. The results of solid-state photoluminescence (PL) tests of **3**−**5** display the characteristic emitting bands stemming from intra4f transitions of Ln ions. Furthermore, energy transfer (ET) phenomenon of the O → W ligand-to-metal charge transfer (LMCT) transitions sensitizing the emission of Ho^{3+} ions in **5** was also probed.

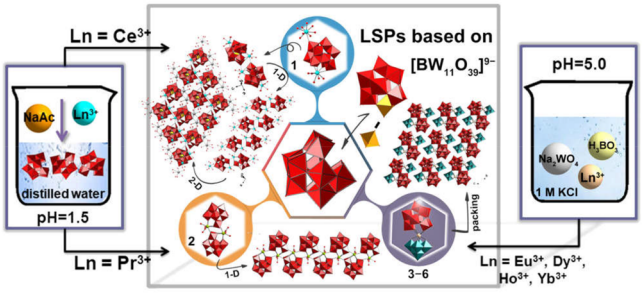

Figure 1. Summary of schematic synthetic processes of **1**−**6**.

RESULTS AND DISCUSSION

Structure Discussion. Powder X-ray diffraction (XRD) spectra for **1**−**6** are consistent with single-crystal XRD spectra, signifying that all of the samples are pure. (Figure S1).

The molecular structure unit of **1** is composed of a $[Ce(H_2O)_8][(\alpha\text{-}BW_{11}O_{39})Ce(H_2O)_3]^{3-}$ (**1a**) polyoxoanion, a K^+ ion, two H^+ ions, and 14 crystal waters. **1a** (Figure 2a)

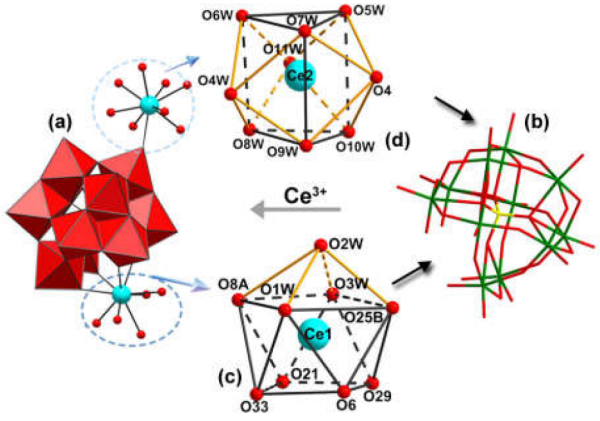

Figure 2. (a) Molecular structure unit of **1**. (b) The {BW_{11}} unit. (c, d) Coordination configurations of $Ce1^{3+}$ and $Ce2^{3+}$ ions in **1**. Symmetry codes: (A) $1-x, 1-y, -z$; (B) $-x, 1-y, -z$. O: red, Ce: turquoise, B: yellow, {WO_6}: red.

can be described as a hydrated $[Ce(H_2O)_8]^{3+}$ ligand with a 1:1 type mono-Ln-substituted fragment with a $Ce1^{3+}$ cation incorporated to the "cap" vacant site of the {BW_{11}} subunit. In {BW_{11}} (Figure 2b), the B atom resides in the center of {BO_4} tetrahedron and is surrounded by three μ_4-O atoms from three vertex-sharing {W_3O_{13}} triads and one μ_3-O atom from an edging-sharing {W_2O_{10}} dimer [B−O: 1.470(17)−1.540(16) Å, ∠O−B−O: 105.2(10)−113.4(11)°]. Two crystallographically unique Ce^{3+} cations exist in the complex unit, which have different coordination environments. The $Ce1^{3+}$ cation occupies the defect site of {BW_{11}} in the "cap" region to form the $[(\alpha\text{-}BW_{11}O_{39})Ce(H_2O)_3]^{6-}$ fragment, adopting a seriously contorted monocapped square antiprism (Figure 2c) bonding to six terminal oxygen atoms from three different {BW_{11}} moieties [Ce−O: 2.479(10)−2.536(9) Å], as well as three water molecules [Ce−O: 2.567(12)−2.636(11) Å]. The $Ce2^{3+}$ center is embedded in a twisted tricapped triangular prism (Figure 2d) defined by one terminal oxygen

DOI: 10.1021/acs.cgd.9b01290
Cryst. Growth Des. 2020, 20, 362−369

atom from $\{BW_{11}\}$ moieties [Ce−O: 2.537(10) Å] and eight water molecules [Ce−O: 2.52(2)−2.58(2) Å].

Intriguingly, two **1a** units can be linked together by $Ce1^{3+}$ cations to form a Ce-substituted double-Keggin-type entity $\{[Ce(H_2O)_8][(\alpha\text{-}BW_{11}O_{39})Ce(H_2O)_3]\}_2^{6-}$ (**1b**) (Figure 3a).

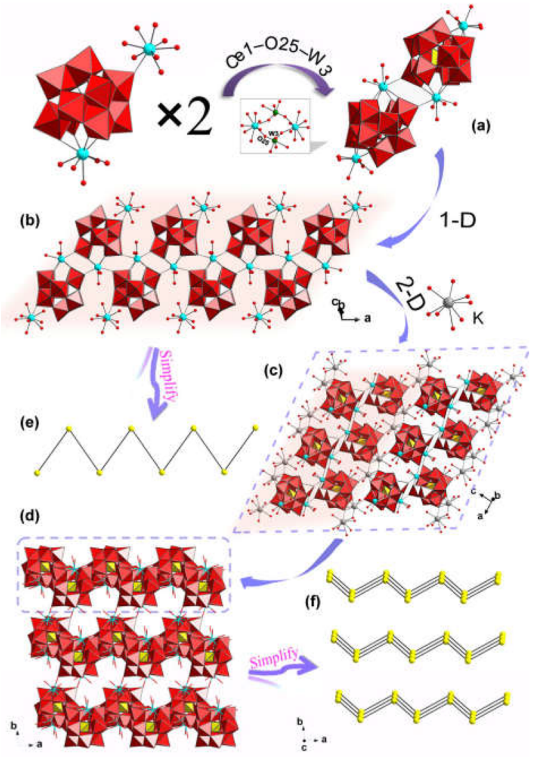

Figure 3. (a) View of **1b**. (b) The 1-D chain in **1**. (c) The 2-D layer of **1**. (d) Packing arrangement of **1** along *c* axis. (e) View of the simplified 1-D chain in **1**. (f) View of the simplified packing of **1** along *c* axis. O: red, Ce: turquoise, B: yellow, K: gray-50%, W: green, $\{WO_6\}$: red, $\{BO_4\}$: gold.

This dimeric **1b** entity in **1** possesses a centric head-to-head architecture and can be regarded as a combination of two identical symmetrically related **1a** moieties by means of the bridging role of two $Ce1^{3+}$ cations. Subsequently, adjacent **1b** entities are joined together to yield a 1-D zigzag chain by the assistance of Ce−O−W bonds (Figure 3b). Furthermore, these wavelike chains are interconnected in the −A-A-A− packing mode by K^+ cations, and then a novel two-dimensional (2-D) layered structure based on $\{BW_{11}\}$ as well as Ce^{3+} cations can be obtained (Figure 3c). Herein, the functionality of K^+ cations also exhibits an arrestive bridging effect except the common role of charge compensation. Consequently, 1-D coordination polymeric chains are linked together through the K−O−W bridges, giving rise to a distinctive 2-D extended framework. Synchronously, the packing arrangement of this 2-D layer is shown in Figure 3d−f.

When Pr^{3+} was utilized in place of Ce^{3+} under similar conditions with **1**, then **2** can be obtained. Different than **1**, **2** reveals a 1-D wavelike chain without hanging $[Pr(H_2O)_8]^{3+}$ ions. The molecular unit of **2** includes a mono-Pr^{III}-substituted Keggin $[(\alpha\text{-}BW_{11}O_{39})Pr(H_2O)_3]^{6-}$ segment (Figure 4a), two K^+ ions, two Na^+ ions, a H^+ ion, and 15 crystal waters. Ulteriorly, Pr^{3+} ions function as bridges between two neighboring $\{BW_{11}\}$ subunits to create a centrosymmetric

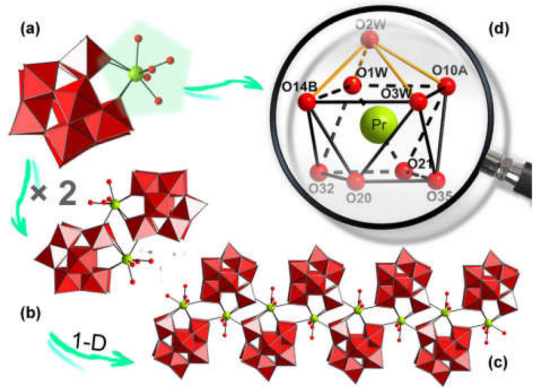

Figure 4. (a) Molecular structure unit of **2**. (b) View of $[(\alpha\text{-}BW_{11}O_{39})Pr(H_2O)_3]_2^{12-}$. (c) View of the 1-D chain in **2**. (d) Coordination geometry of the Pr^{3+} cation in **2**. Symmetry codes: (A) $1-x, 2-y, -z$; (B) $1-x, 1-y, -z$. O: red, Pr: lime, B: yellow, $\{WO_6\}$: red.

Pr^{III}-substituted double-Keggin-type polyoxoanion $[(\alpha\text{-}BW_{11}O_{39})Pr(H_2O)_3]_2^{12-}$ (Figure 4b), which ultimately are interconnected each other via W−O−Pr−O−W linkages to construct a 1-D extended chain (Figure 4c). The Pr^{3+} ion is positioned at the lacunary site of monolacunary Keggin $\{BW_{11}\}$ subunit and is coordinated to three aqua molecules [Pr−O: 2.532(9)−2.607(9) Å] and three adjacent $\{BW_{11}\}$ subunits [Pr−O: 2.445(8)−2.510(8) Å] in a highly distorted monocapped square antiprism (Figure 4d). Notably, the dimeric $[(\alpha\text{-}BW_{11}O_{39})Pr(H_2O)_3]_2^{12-}$ polyoxoanion in **2** is somewhat similar to the dimeric $[Ce_2(BW_{11}O_{39})_2(H_2O)_6]^{12-}$ polyoxoanion addressed by Sousa et al., which bears the alike 1-D chain framework. The Pr^{3+} cation in **2** has a monocapped square antiprism differing from the tricapped triangular prism of the Ce^{3+} ion in $[Ce_2(BW_{11}O_{39})_2(H_2O)_6]^{12-}$.[33]

Compounds **3**−**6** are isostructural, and **5** is discussed here. The architecture of **5** exhibits a discrete Ln-substituted BT containing a monovacant Keggin $\{BW_{11}\}$ subunit and a monovacant Lindqvist $[W_5O_{18}]^{6-}$ subunit (Figure 5a). To our knowledge, Yamase and collaborators reported the similar structure.[35] The monovacant $\{BW_{11}\}$ subunit acts as a tetradentate ligand (Figure 5b) coordinating with the Ho^{3+} center by its four unsaturated oxygen atoms. Analogously, the $[W_5O_{18}]^{6-}$ subunit that is derived from isopolyoxotungstate $[W_6O_{19}]^{2-}$ anion can also serve as a chelate tetradentate ligand (Figure 5c) linking to the Ln center by its four unsaturated oxygen atoms. Interestingly, eight oxygen atoms from monovacant Keggin and Lindqvist subunits can build two bottom planes (Figure 5d) of a square antiprism. Therefore, the Ho^{3+} ion is anchored in the square antiprism geometry (Figure 5e) [Ho−O: 2.315(7)−2.448(7) Å]. As displayed in Figure 5f, $[(W_5O_{18})Ho(\alpha\text{-}BW_{11}O_{39})]^{12-}$ units are arranged in the order of −ABAB−; moreover, adjacent units adopt an antiparallel arrangement pattern; that is, small $[W_5O_{18}]^{6-}$ building blocks and large $\{BW_{11}\}$ units are alternately distributed, which could effectively reduce the steric hindrance and favor the closest packing of the overall structure.

PL Studies. As is well-known, since the excellent optical properties of Ln ions like sharp characteristic emissions, good chemical stability, high quantum efficiency, and long luminescent lifetimes can be well-retained in their diversiform ramification, LnSPs synchronously endowed with merits of parent POM fragments and Ln ions show considerable interest

DOI: 10.1021/acs.cgd.9b01290
Cryst. Growth Des. 2020, 20, 362−369

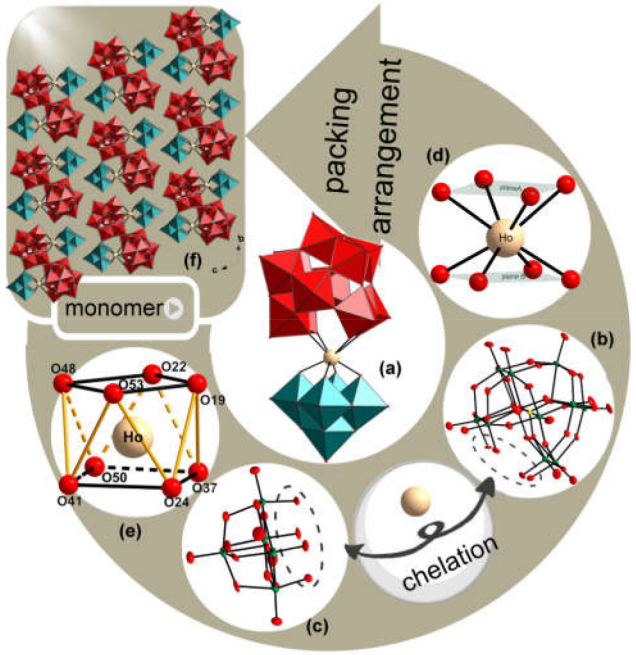

Figure 5. (a) Molecular structure of **5**. (b) Coordination geometry of the Ho^{3+} cation in **5**. (c) View of the $[W_5O_{18}]^{6-}$ subunit. (d) View of the $\{BW_{11}\}$ subunit. (e) Coordination sphere of the Ho^{3+} cation. (f) The packing arrangement of **5** along *a* axis. O: red, Ho: tan, B: yellow, $\{BW_{11}\}$: red, $\{[W_5O_{18}]^{6-}\}$: teal.

in lasers, light-emitting diodes, cathode rays, plasma displays, optical fibers, near-infrared (NIR)-emitting materials, and sensory probes.[36−38] Herein, solid-state PL properties of **3**−**5** were studied at ambient temperature.

The emitting spectrogram of **3** (Figure 6a) under 395 nm excitation displays five Eu^{3+} characteristic luminescent bands at 580, 595, 621, 652, and 702 nm, corresponding to the $^5D_0 \rightarrow {}^7F_J$ (J = 0−4) transitions, respectively. Magnetic dipole $^5D_0 \rightarrow {}^7F_{1,3}$ transitions are insusceptible to regional circumstances, whereas electric dipole $^5D_0 \rightarrow {}^7F_{0,2,4}$ transitions are fairly susceptive to regional circumstances.[39] Generally, the $^5D_0 \rightarrow {}^7F_0$ emission is severely forbidden in a symmetric circumstance, but the faint $^5D_0 \rightarrow {}^7F_0$ emission at 580 nm can be observed in **3**, which testifies that Eu^{3+} ions dwell in the relatively lower symmetric circumstances. The $^5D_0 \rightarrow {}^7F_1$ transition at 595 nm is preponderant in a centrosymmetric circumstance. However, the $^5D_0 \rightarrow {}^7F_2$ transition at 621 nm is the strongest in a non-centrosymmetric circumstance, and its emitting intensity rises with the decreasing of the regional symmetry of the Eu^{3+} ion.[40,41] Besides, the $^5D_0 \rightarrow {}^7F_2/{}^5D_0 \rightarrow {}^7F_1$ intensity specific value is generally functioning as a measure of detecting the coordinate circumstance and regional symmetry of Eu^{3+} ions.[42] Here, the $^5D_0 \rightarrow {}^7F_2/{}^5D_0 \rightarrow {}^7F_1$ intensity specific value of ca. 3.6 for **3** indicates the low-symmetry of the Eu^{3+} cation. What's more, the excited spectrogram through detecting 621 nm emission is presented in Figure S3, and the most intense peak is located at 395 nm ($^7F_0 \rightarrow {}^5L_6$), while other weak peaks are observed at 362 ($^7F_0 \rightarrow {}^5D_4$), 381($^7F_0 \rightarrow {}^5G_3$), and 414 nm ($^7F_0 \rightarrow {}^5D_3$).[43] Otherwise, the luminescence lifespan profile for **3** conforms to a first-order exponential function $I = A\exp(-t/\tau)$ (Figure 6b), generating τ of 1478.08 μs (Table S2).

Under 366 nm excitation, the emitting spectrogram for **4** (Figure 6c) demonstrates three apparent peaks assigned to Dy^{3+} $^4F_{9/2} \rightarrow {}^6H_{15/2}$ (480 nm), $^4F_{9/2} \rightarrow {}^6H_{13/2}$ (573 nm), and $^4F_{9/2} \rightarrow {}^6H_{11/2}$ (663 nm). Obviously, the strongest emitting peak is located at 573 nm, whose intensity is far greater than other peaks to some extent. Its excited spectrogram (Figure S4), on the basis of supervising the $^4F_{9/2} \rightarrow {}^6H_{13/2}$ transition at 573 nm, displays four prominent peaks at 342, 366, 388, and 428 nm, which are severally attributed to Dy^{3+} $^6H_{15/2} \rightarrow {}^6P_{7/2}$, $^6H_{15/2} \rightarrow {}^6P_{5/2}$, $^6H_{15/2} \rightarrow {}^4I_{13/2}$, and $^6H_{15/2} \rightarrow {}^4G_{11/2}$.[44] Similarly, the lifespan curve for **4** (Figure 6d) was determined and abides by a first-order exponential function with τ of 47.63 μs. (Table S2).

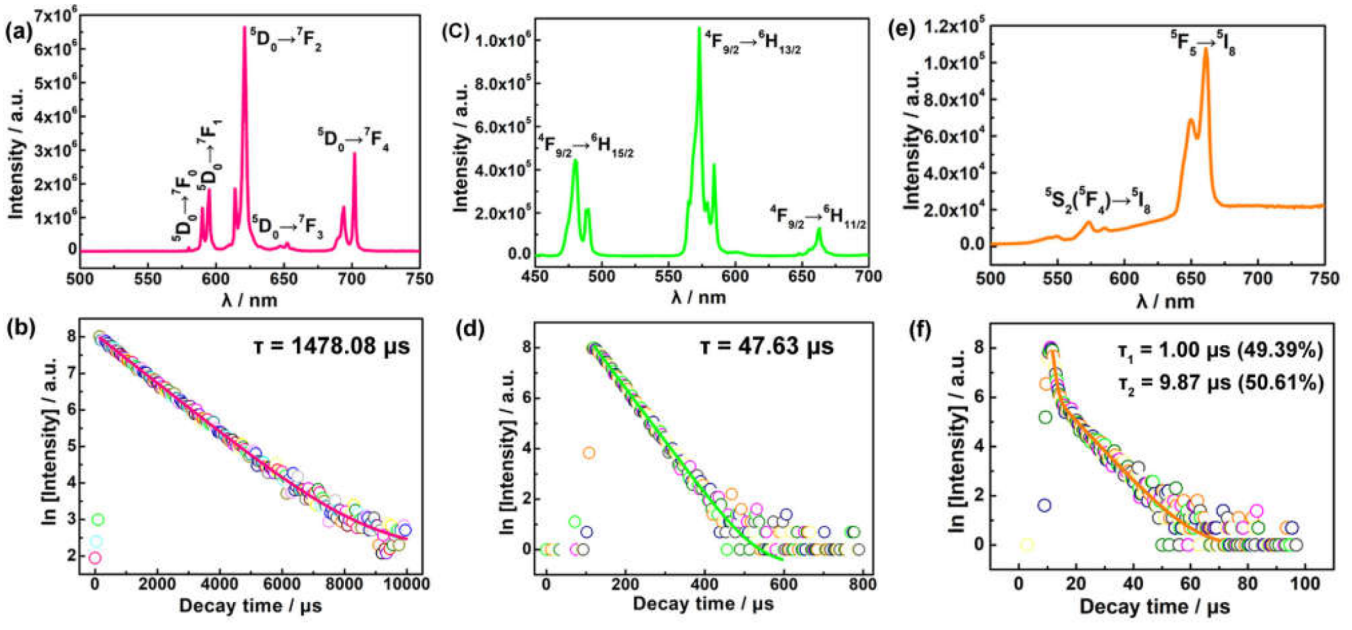

Figure 6. (a, c, e) Emitting spectrograms for **3** (λ_{ex} = 395 nm), **4** (λ_{ex} = 366 nm), and **5** (λ_{ex} = 454 nm). (b, d, f) Luminescence decay profiles for **3**, **4**, and **5**.

DOI: 10.1021/acs.cgd.9b01290
Cryst. Growth Des. 2020, 20, 362−369

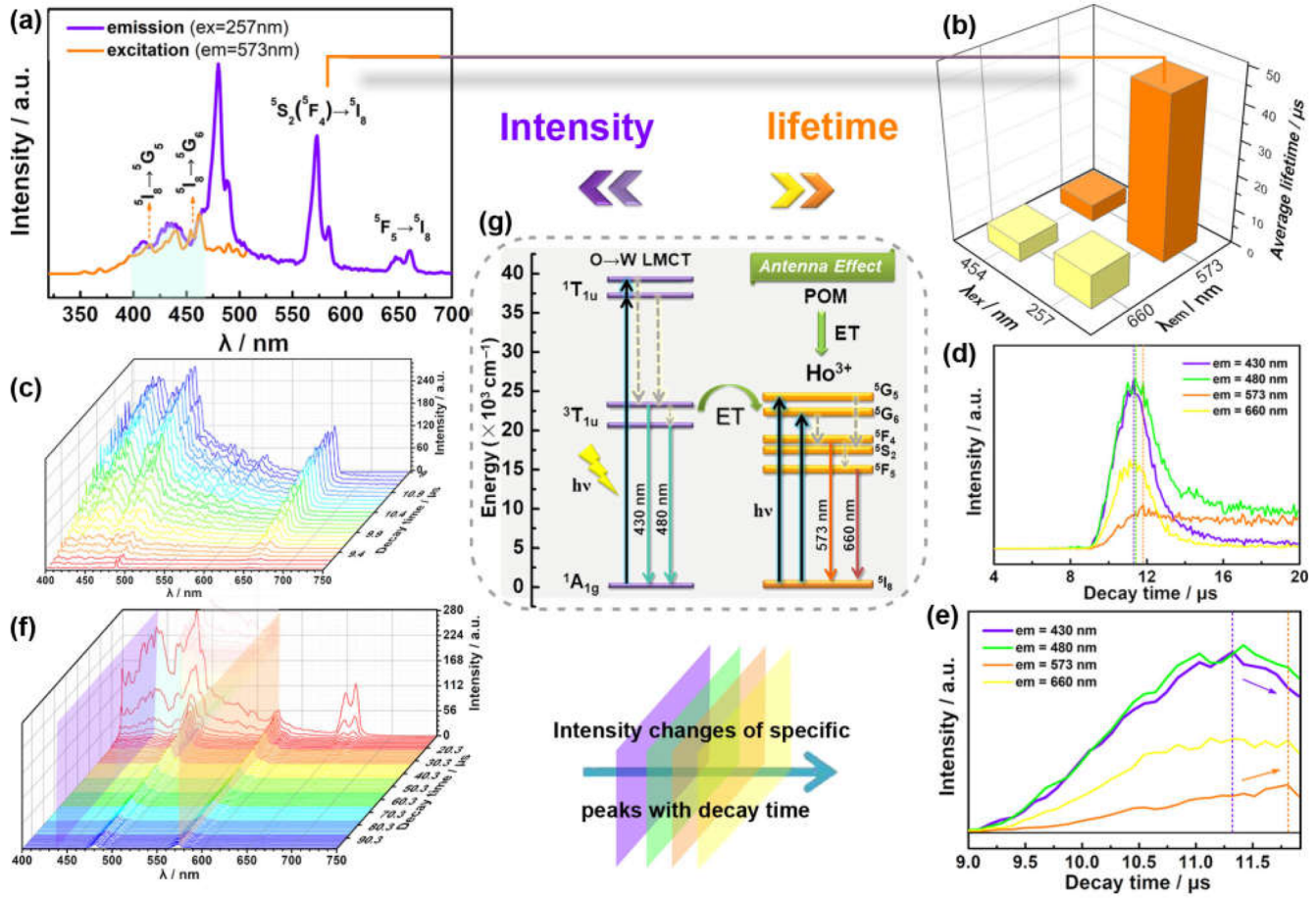

Figure 7. (a) Luminescent spectrogram for **5** in 400−750 nm under 257 nm excitation and the excited spectrogram for **5** in 320−500 nm based on supervising 573 nm emission. (b) Average lifetimes comparison for Ho^{3+} $^5S_2(^5F_4) \rightarrow {}^5I_8$ and $^5F_5 \rightarrow {}^5I_8$ emission peaks upon excitations at 257 and 454 nm. (c) The 9−11.3 μs TRES spectra for **5** on base of 257 nm excitation. (d) Intensity comparison of emitting peaks at 430, 480, 573, and 660 nm with decay time. (e) An enlarged view of Figure 6d (the decay time range is 9−11.9 μs). (f) The 11.3−100 μs TRES spectra for **5** on base of 257 nm excitation. (g) Diagrammatic energy-level drawing indicating ET process from BT units to Ho^{3+} centers. Solid lines stand for radiation procedure, and dotted lines are on behalf of nonradiative procedure.

The emitting spectrum for **5** (Figure 6e) under excitation at 454 nm gives birth to the orange emission of Ho^{3+} ions severally appearing at 573 and 660 nm. The strongest emission at 660 nm together with a splitting peak around 650 nm are assigned to Ho^{3+} $^5F_5 \rightarrow {}^5I_8$, while the 573 nm peak is attributable to Ho^{3+} $^5S_2(^5F_4) \rightarrow {}^5I_8$. The excited spectrum of **5** (Figure S5) based on supervising 660 nm emission is dominated by the $^5I_8 \rightarrow {}^5G_6$ transition at 454 nm, whereas the observable weak peak at 418 nm corresponds to $^5I_8 \rightarrow {}^5G_5$.[45] The PL lifetime profile for **5** based on the 660 nm emitting peak was also performed, and it can conform to the second-order exponential function (Figure 6f), affording τ_1 = 1.00 μs (49.39%) and τ_2 = 9.87 μs (50.61%); and the average lifetime τ^* is 5.49 μs, and an agreement coefficient χ^2 is 1.031 (Table S2).

It can be known from the aforesaid structural analysis that one crystallographically unique Ln cation exists in **3**−**5**. On condition that only the emitting behavior of Ln ions is taken into consideration, their luminescence lifespan profiles should act up to the single exponential equation; however, this case is not in conformity with the experimental result of **5**. As a consequence, we speculate that there is nonignorable effect from BT units during the luminescence procedure for **5**. In an effort to hunt for the source of extra luminescence contribution, the PL-emitting spectrogram and lifespan curve for **6** were collected under identical conditions. For all we know, the Yb^{3+} ion with f^{13} valence electronic configuration has only one featured emitting band in the near-infrared range, so the visible emission for **6** primarily stems from the O → W LMCT of BT fragments. A broad emission band appears between 500 and 750 nm on excitation with a light of 454 nm (Figure S6), while the PL decay profile for **6** (Figure S11a) adheres to a two-order exponential function with τ_1 = 2.84 μs (53.87), τ_2 = 11.03 μs (46.13%), and τ^* = 6.62 μs. Overly, τ^* for **6** (Table S2) is very close to that of **5** (τ = 5.49 μs), elucidating that BT units certainly play an indispensable part in the PL process for **5** (Figure S11a). In addition, the PL properties of **6** were also researched under the same conditions as **3** and **4** (Figures S7−S10, Table S2). Clearly, in comparison with the lifetimes of **3** (1478.08 μs) and **4** (47.63 μs), the lifetime contribution of BT units (6.34 μs) and (6.01 μs) is almost neglectful (Figure S11b).

According to previous reports, POM segments can emit a wide band in 350−550 nm pertaining to the O → W $^3T_{1u} \rightarrow {}^1A_{1g}$ transition.[46,47] As a rule, electrons in tungsten-oxo clusters can be first excited from the $^1A_{1g}$ ground state to the $^1T_{1u}$ excited state and then are relaxed to the low-energy $^3T_{1u}$ excited state, whereas the $^3T_{1u}$ triplet excited state not only can

DOI: 10.1021/acs.cgd.9b01290
Cryst. Growth Des. 2020, 20, 362−369

release energy by means of $^3T_{1u} \rightarrow {}^1A_{1g}$ electron transition but also can transfer energy to some Ln ions with similar energy levels via.[48] Herein, we have indicated that BT units and Ln cations make conjoint contribution in the course of PL behaviors for **3**−**5**. To further probe whether there is energy transfer between BT units and Ln ions, we chose to make a thorough inquiry into the PL spectra and ET behaviors for **5** owing to its relatively weak emission intensity and short decay lifetime approximating to BT units. In the beginning, the PL-emitting spectrogram for **5** in 400−700 nm was probed under the O → W LMCT excitation at 257 nm (Figure S12), where a broad band is displayed varying from 400−500 nm with maximum at 480 nm derived from $^3T_{1u} \rightarrow {}^1A_{1g}$ of BT units (Figure S13), and the typical emitting bands of Ho^{3+} ions assigned to f−f transitions are simultaneously presented in this spectrogram (the violet line in Figure 7a). The excited spectrogram of **5** between 400 and 500 nm also recorded via detecting the $^5S_2(^5F_4) \rightarrow {}^5I_8$ emission at 573 nm and revealed two obvious peaks originating from the characteristic excitation of Ho^{3+} ions (the orange line in Figure 7a). It can be unambiguously observed that the $^3T_{1u} \rightarrow {}^1A_{1g}$ emitting band of BT units can well-superpose with the Ho^{3+} excited peaks, acting as a powerful illustration of the existence of ET between Ln ions and BT units. By comparing emitting spectra taken based on 257 nm excitation from tungsten-oxo clusters and 454 nm excitation of Ho^{3+} $^5F_5 \rightarrow {}^5I_8$ transition, we can clearly find that the $^5S_2(^5F_4) \rightarrow {}^5I_8$ emitting peak at 573 nm is dominant with the $I(^5S_2(^5F_4) \rightarrow {}^5I_8)/I(^5F_5 \rightarrow {}^5I_8)$ emitting intensity ratio of 5.97:1 under 257 nm excitation, whereas the $^5F_5 \rightarrow {}^5I_8$ emitting peak at 660 nm is dominant with the $I(^5S_2(^5F_4) \rightarrow {}^5I_8)/I(^5F_5 \rightarrow {}^5I_8)$ emitting intensity ratio of 0.13:1 under 454 nm excitation, which indirectly manifests that BT units exhibit different sensitization effects on $^5S_2(^5F_4) \rightarrow {}^5I_8$ and $^5F_5 \rightarrow {}^5I_8$ transitions. Upon 257 nm excitation, the part energy from the $^3T_{1u} \rightarrow {}^1A_{1g}$ transition of BT units is reabsorbed by the $^5I_8 \rightarrow {}^5G_5$ and $^5I_8 \rightarrow {}^5G_6$ transitions of Ho^{3+} ions in the nonradiative form in **5**, whereas the $^5S_2(^5F_4) \rightarrow {}^5I_8$ transition receives the most energy from tungsten-oxo clusters, so the peak intensity at 573 nm is more transparently enhanced than that of another peak at 660 nm. Synchronously, comparison of decay lifetimes under different excitation and detection conditions can also prove this point. As demonstrated in Figure 7b, lifetimes of two characteristic peaks are both prolonged to some extent under 257 nm excitation [for the $^5S_2(^5F_4) \rightarrow {}^5I_8$ transition: 4.92 μs → 46.93 μs; the $^5F_5 \rightarrow {}^5I_8$ transition: 5.49 μs → 9.67 μs] (Table S2, Figures S14−S16), but it can be intuitively seen that the lifetime extension of $^5S_2(^5F_4) \rightarrow {}^5I_8$ transition is much more than that of $^5F_5 \rightarrow {}^5I_8$ transition, which provides some evidence that the sensitization of BT units toward the $^5S_2(^5F_4) \rightarrow {}^5I_8$ emission is larger than the $^4F_{9/2} \rightarrow {}^6H_{13/2}$ emission. Furthermore, the time-resolved emission spectrum (TRES) tests of **5** were performed upon excitation with a light of 257 nm in 400−750 nm. Obviously, the broad emission band varying 400−500 nm arising from O → W LMCT triplet state in BT units appears as the bimodal form during the course of excitation of tungsten-oxo clusters (centered at 430 and 480 nm, respectively) (Figure 7c), and the huge ravine falls at ∼454 nm, which can be explained that Ho^{3+} $^5I_8 \rightarrow {}^5G_6$ transition absorbs energy from the $^3T_{1u} \rightarrow {}^1A_{1g}$ transition of BT units. As time elapses, emitting peaks at 430, 480, 573, and 660 nm emerge at 9.0 μs and arrive at the maxima at 11.3, 11.4, 11.8, and 11.4 μs, respectively (Figure 7d). In other words, the intensity of the wide emitting band (400−470 nm) centered at 430 nm begins to weaken at 11.3 μs; at the same time, the intensities of two characteristic emitting peaks centered at 573 and 660 nm belonging to Ho^{3+} ions further increase, consolidating the existence of ET between BT units and Ho^{3+} ions (Figure 7e, Figure S17). In terms of the emitting band of tungsten-oxo clusters, the sunken band (400−470 nm) gradually appears with time going by, and the broad band ends up with only one relatively sharp peak, resulting from the energy absorption of $^5I_8 \rightarrow {}^5G_5$ and $^5I_8 \rightarrow {}^5G_6$ transitions of the Ho^{3+} cation. As for two emitting peaks deriving from f−f transitions, the peak at 660 nm from $^5F_5 \rightarrow {}^5I_8$ transition is prominent in the infancy of decaying, but the peak of $^5S_2(^5F_4) \rightarrow {}^5I_8$ transition at 573 is dominant, and the peak at 660 nm is feeble at ca. 30 μs, which signifies the PL decay rate of the emitting peak at 660 nm is much faster than that of the emitting peak at 573 nm, coinciding with the conclusion that more energy migrates to the $^5S_2(^5F_4) \rightarrow {}^5I_8$ transition and less to the $^5F_5 \rightarrow {}^5I_8$ transition (Figure 7f). Figure 7g reveals the possible ET process between BT units to Ho^{3+} ions, which well agrees with experimental results. In the first place, the POM skeleton as a sensitizer can absorb energy to force electrons to transfer from $^1A_{1g}$ to $^1T_{1u}$, whereafter, electrons at $^1T_{1u}$ jump to $^3T_{1u}$ by fast relaxation. Hereafter, in addition to releasing energy by returning to $^1A_{1g}$ through a radiative transition, there is still part energy transfer to $^5G_5$ and $^6G_5$ of Ho^{3+} ions, thereby promoting the $^5S_2(^5F_4) \rightarrow {}^5I_8$ and $^5F_5 \rightarrow {}^5I_8$ transitions. Since the energy corresponding to the broad band in the region of 400−470 centered at 430 nm is very close to that of $^5I_8 \rightarrow {}^5G_5$ and $^5I_8 \rightarrow {}^5G_6$ of Ho^{3+} cation, the ET efficiency is relatively high leading to an obvious phenomenon that the relevant band shows much shorter excited time and much faster decay rate than the peak at 480 nm.

We may find that **3**−**5** possess the relatively long decay lifetime, which may be mainly related to the two following reasons: (i) There is no obvious O−H frequency oscillators from aqua ligands impairing the emission of Ln ions. The oxygen atoms located at the defect sites of $[W_5O_{18}]^{6-}$ and $\{BW_{11}\}$ segments occupy all the coordination sites of Ln ions, precluding the coordination of quenching species such as water molecules to Ln centers, thereby reducing nonradiative decay processes;[49] (ii) BT units can act as antenna ligands upon photoexcitation to transfer energy from the O → M LMCT triplet state to Ln ions, leading to prolonging lifetimes of Ln ions. Exceptionally, the PL decay lifetime of **5** can even be extended to 46.93 μs under the O → W LMCT excitation at 257 nm (the average lifetime is 5.49 μs under the strongest f−f transition excitation at 454 nm) (Table S2).

The CIE 1931 diagram has been widely applied to gauge all possible colors by the combination of three primary colors (red, blue, and green), offering a pervasive method to quantify the tunability of the emission wavelength as well as the change of the emission intensity, and to acquire a good knowledge of the trueness of color for applications in light-emitting devices.[50] In the CIE diagram, the chromaticity coordinate x represents the red-to-blue ratio, while y represents the green-to-blue ratio. According to these two coordinates, the exact emission color of a compound can be easily determined when the white light emission is centrally located with the standard chromaticity coordinates (x = 0.333 33, y = 0.333 33). Here, color coordinates for **3**−**5** on the basis of their corresponding emission spectra are (0.662 67, 0.336 99), (0.381 87,

DOI: 10.1021/acs.cgd.9b01290
Cryst. Growth Des. 2020, 20, 362−369

0.428 87), and (0.590 14, 0.405 08), respectively. Hereinto, **3**−**5** display reddish-orange, yellow-green, and orange emissions (Figure S18).

CONCLUSIONS

In summary, three types of novel POMs **1**−**6** based on Keggin-type monovacant $\{BW_{11}\}$ units and Ln cations were successfully synthesized. Adjacent molecular segments in **1** are connected via Ce−O−W bonds into the 1-D chain, and neighboring 1-D chains are combined together to form a fascinating 2-D extended framework by K^+ bridges. **2** owns the analogical 1-D chain arrangement formed by adjacent molecular segments via Pr^{3+} ions. **3**−**6** exhibit a fascinating dimeric Ln-substituted BT architecture contaning one monovacant Keggin $\{BW_{11}\}$ and Lindqvist $[W_5O_{18}]^{6-}$ fragment that are fused together by an Ln core. Compounds **3**−**5** exhibit the characteristic emissions from Ln centers corresponding to the inherent f−f transitions. It is noteworthy that BT fragments take an indispensable part in the course of PL emission. Additionally, a prominent feature of **3**−**5** is that they own a relatively long luminescence lifetime, which is primarily because of the chelation of proximal ligands with Ln cations interfering with the coordination of quenching species like water molecules to Ln centers. Simultaneously, the existence of ET from BT segments to Ln centers also plays a pivotal role in prolonging the decay lifetime of **6**. Overall, the success in synthesizing **1**−**6** not only provides more candidates for the discovery of good performance materials but the preliminary property studies also laid the foundation for subsequent in-depth exploration. In the following work, we will try to introduce a variety of TM cations into our system to fabricate unprecedented heterometallic BTs. Apart from this, multipurpose organic ligands will be used as luminescence sensitizers and structure-directors to fabricate novel inorganic−organic hybrid LnSBTs with improved luminescence activities.

ASSOCIATED CONTENT

Supporting Information

The Supporting Information is available free of charge at https://pubs.acs.org/doi/10.1021/acs.cgd.9b01290.

IR spectra and PXRD patterns for **1**−**6**, luminescence figures of **3**−**6**; crystal data and BVS calculations for **1**−**6** (PDF)

Accession Codes

CCDC 1940093−1940098 contain the supplementary crystallographic data for this paper. These data can be obtained free of charge via www.ccdc.cam.ac.uk/data_request/cif, or by emailing data_request@ccdc.cam.ac.uk, or by contacting The Cambridge Crystallographic Data Centre, 12 Union Road, Cambridge CB2 1EZ, UK; fax: +44 1223 336033.

AUTHOR INFORMATION

Corresponding Authors

*E-mail: ljchen@henu.edu.cn. (L.J. Chen)
*E-mail: zhaojunwei@henu.edu.cn. (J.W. Zhao)

ORCID

Junwei Zhao: 0000-0002-7685-1309

Notes

The authors declare no competing financial interest.

ACKNOWLEDGMENTS

This work was supported by the National Natural Science Foundation of China (21871077, 21571048, 21671054, 21771052) and the Program for Innovation Teams in Science and Technology in Universities of Henan Province (20IRTSTHN004).

REFERENCES

(1) Bösing, M.; Nöh, A.; Loose, I.; Krebs, B. Highly efficient catalysts in directed oxygen-transfer processes: synthesis, structures of novel manganese- containing heteropolyanions, and applications in regioselective epoxidation of dienes with hydrogen peroxide. *J. Am. Chem. Soc.* **1998**, *120*, 7252.

(2) AlDamen, M. A.; Clemente-Juan, J. M.; Coronado, E.; Martí-Gastaldo, C.; Gaita-Arino, A. Mononuclear lanthanide single-molecule magnets based on polyoxometalates. *J. Am. Chem. Soc.* **2008**, *130*, 8874.

(3) Aparicio-Anglés, X.; Miro, P.; Clotet, A.; Bo, C.; Poblet, J. M. Polyoxometalates adsorbed on metallic surfaces: immediate reduction of $[SiW_{12}O_{40}]^{4-}$ on Ag (100). *Chem. Sci.* **2012**, *3*, 2020.

(4) Liu, J. C.; Han, Q.; Chen, L. J.; Zhao, J. W.; Streb, C.; Song, Y. F. Aggregation of giant cerium−bismuth tungstate clusters into a 3D porous framework with high proton conductivity. *Angew. Chem., Int. Ed.* **2018**, *57*, 8416.

(5) Bijelic, A.; Aureliano, M.; Rompel, A. The antibacterial activity of polyoxometalates: structures, antibiotic effects and future perspectives. *Chem. Commun.* **2018**, *54*, 1153.

(6) Najafi, A.; Mirzaei, M.; Mague, J. T. Structural scope of six new layered to pillar-layered hybrid inorganic−organic networks bearing $[BW_{12}O_{40}]^{5-}$ and lanthanoid-cluster; database study toward ligand role in assemblies. *CrystEngComm* **2016**, *18*, 6724.

(7) Wang, S.; Yu, K.; Wang, B.; Wang, L.; Wang, C. X.; Zhang, H.; Wang, C. M.; Zhou, B. B. Construction of two novel borotungstates modified by different ligands connected with single/double bridges. *New J. Chem.* **2016**, *40*, 7011.

(8) Liu, J. C.; Yu, J.; Han, Q.; Wen, Y.; Chen, L. J.; Zhao, J. W. First quadruple-glycine bridging mono-lanthanide-substituted borotungstate hybrids. *Dalton Trans.* **2016**, *45*, 16471.

(9) Li, Y. W.; Li, Y. G.; Wang, Y. H.; Feng, X. J.; Lu, Y.; Wang, E. B. A new supramolecular assembly based on triple-Dawson-type polyoxometalate and 3d-4f heterometallic cluster. *Inorg. Chem.* **2009**, *48*, 6452.

(10) Dolbecq, A.; Compain, J. D.; Mialane, P.; Marrot, J.; Rivière, E.; Sécheresse, F. Water substitution on iron centers: from 0D to 1D sandwich type polyoxotungstates. *Inorg. Chem.* **2008**, *47*, 3371.

(11) Zheng, S. T.; Zhang, J.; Yang, G. Y. Designed synthesis of POM−organic frameworks from $\{Ni_6PW_9\}$ building blocks under hydrothermal conditions. *Angew. Chem., Int. Ed.* **2008**, *47*, 3909.

(12) Zhao, J. W.; Jia, H. P.; Zhang, J.; Zheng, S. T.; Yang, G. Y. A combination of lacunary polyoxometalates and high-nuclear transition-metal clusters under hydrothermal conditions. Part II: From double cluster, dimer, and tetramer to three-dimensional frameworks. *Chem. - Eur. J.* **2007**, *13*, 10030.

(13) Lu, Y.; Xu, Y.; Li, Y. G.; Wang, E. B.; Xu, X. X.; Ma, Y. New polyoxometalate compounds built up of lacunary Wells−Dawson anions and trivalent lanthanide cations. *Inorg. Chem.* **2006**, *45*, 2055.

(14) Rocchiccioli-Deltcheff, C.; Fournier, M.; Franck, R.; Thouvenot, R. Vibrational investigations of polyoxometalates. 2. Evidence for anion-anion interactions in molybdenum(VI) and tungsten(VI) compounds related to the Keggin structure. *Inorg. Chem.* **1983**, *22*, 207.

(15) Fletcher, H.; Allen, C. C.; Burns, R. C.; Craig, D. C. Pentapotassium dodecatungstoborate (III) hexadecahydrate. *Acta Crystallogr., Sect. C: Cryst. Struct. Commun.* **2001**, *57*, 505.

(16) Xu, J. J.; Volfova, H.; Mulder, R. J.; Goerigk, L.; Bryant, G.; Riedle, E.; Ritchie, C. Visible-light-driven "on"/"off" photochromism of a polyoxometalate diarylethene coordination complex. *J. Am. Chem. Soc.* **2018**, *140*, 10482.

DOI: 10.1021/acs.cgd.9b01290
Cryst. Growth Des. 2020, 20, 362−369

(17) An, H. Y.; Wang, E. B.; Li, Y. G.; Zhang, Z. M.; Xu, L. A functionalized polyoxometalate by hexanuclear copper−amino acid coordination complexes. *Inorg. Chem. Commun.* **2007**, *10*, 299.
(18) An, H. Y.; Wang, E. B.; Xiao, D. R.; Li, Y. G.; Su, Z. M.; Xu, L. Chiral 3D architectures with helical channels constructed from polyoxometalate clusters and copper−amino acid complexes. *Angew. Chem., Int. Ed.* **2006**, *45*, 904.
(19) Reinoso, S.; Dickman, M. H.; Matei, M. F.; Kortz, U. 13-Tungstoborate stabilized by an organostannoxane hexamer. *Inorg. Chem.* **2007**, *46*, 4383.
(20) Korenev, V. S.; Abramov, P. A.; Vicent, C.; Mainichev, D. A.; Floquet, S.; Cadot, E.; Sokolov, M. N.; Fedin, V. P. Trapping $\{BW_{12}\}_2$ tungstoborate: synthesis and crystal structure of hybrid $[\{(H_2BW_{12}O_{42})_2O\}\{Mo_6O_6S_6\ (OH)_4(H_2O)_2\}]^{14-}$ anion. *Dalton Trans.* **2012**, *41*, 14484.
(21) Leclerc-Laronze, N.; Marrot, J.; Thouvenot, R.; Cadot, E. Structural link between giant molybdenum oxide based ions and derived Keggin structure: modular assemblies based on the $[BW_{11}O_{39}]^{9-}$ ion and pentagonal $\{M'M_5\}$ units (M′ = W; M = Mo,W). *Angew. Chem., Int. Ed.* **2009**, *48*, 4986.
(22) Reinoso, S.; Vitoria, P.; San Felices, L.; Gutiérrez-Zorrilla, J. M. Diiron(III)- containing 23-tungsto-2-borate: first evidence of 3d metal substitution in the $\{BW_{13}\}$ framework. *Eur. J. Inorg. Chem.* **2013**, *2013*, 1644.
(23) Niu, Y. J.; Liu, B.; Xue, G. L.; Hu, H. M.; Fu, F.; Wang, J. W. A new sandwich polyoxometalate based on Keggin-type monolacunary polyoxotungstoborate anion, $[Zr(\alpha\text{-}BW_{11}O_{39})_2]^{14-}$. *Inorg. Chem. Commun.* **2009**, *12*, 853.
(24) Zhao, J. W.; Song, Y. P.; Ma, P. T.; Wang, J. P.; Niu, J. Y. Hydrothermal syntheses, crystal structures and properties of 0-D, 1-D and 2-D organic−inorganic hybrid borotungstates constructed from Keggin-type heteropolyanion $[\alpha\text{-}BW_{12}O_{40}]^{5-}$ and transition-metal complexes. *J. Solid State Chem.* **2009**, *182*, 1798.
(25) Qi, J. M.; Wang, H. L.; Gao, L. H.; Lin, H.; Wang, K. Z. A new inorganic−organic hybrid film based on a terpyridyl ruthenium (II) complex and $[BW_{11}Zn(H_2O)O_{39}]^{7-}$. *Mater. Lett.* **2015**, *153*, 33.
(26) An, H. Y.; Zheng, H.; Xu, T. Q.; He, C.; et al. Two new hybrid architectures based on polyoxometaloborates and imidazole fragments. *Z. Anorg. Allg. Chem.* **2010**, *636*, 2016.
(27) Wang, X.; Zhang, M. M.; Hao, X. L.; Wang, Y. H.; Wei, Y.; Liang, F. S.; Xu, L. J.; Li, Y. G. Polyoxometalate-induced new self-assemblies based on copper ions and bichelate-bridging ligands. *Cryst. Growth Des.* **2013**, *13*, 3454.
(28) Ding, Y.; Chen, H. L.; Chen, W. L.; Wang, E. B.; Meng, J. X. Synthesis, structures and electrochemical properties of four organic−inorganic hybrid polyoxometalates constructed from polyoxotungstate clusters and transition metal complexes. *Transition Met. Chem.* **2009**, *34*, 281.
(29) Pearson, R. G. Hard and soft acids and bases. *J. Am. Chem. Soc.* **1963**, *85*, 3533.
(30) Binnemans, K. Lanthanide-based luminescent hybrid materials. *Chem. Rev.* **2009**, *109*, 4283.
(31) Ballardini, R.; Chiorboli, E.; Balzani, V. Photophysical properties of $Eu(SiW_{11}O_{39})_2^{13-}$ and $Eu(BW_{11}O_{39})_2^{15-}$. *Inorg. Chim. Acta* **1984**, *95*, 323.
(32) Sousa, F. L.; Ferreira, A.; Sa Ferreira, R. A.; Cavaleiro, A. M. V.; Carlos, L. D.; Nogueira, H. I. S.; Rocha, J.; Trindade, T. Lanthanopolyoxo- tungstoborates: synthesis, characterization, and layer-by-layer assembly of europium photoluminescent nanostructured films. *J. Nanosci. Nanotechnol.* **2004**, *4*, 214.
(33) Sousa, F. L.; Almeida Paz, F. A.; Granadeiro, C. M. C. E.; Cavaleiro, A. M. V.; Rocha, J.; Klinowski, J.; Nogueira, H. I. S. The first one-dimensional lanthanopolyoxotungstoborate. *Inorg. Chem. Commun.* **2005**, *8*, 924.
(34) An, H. Y.; Han, Z. B.; Xu, T. Q. Three-dimensional architectures based on lanthanide-substituted double-Keggin-type polyoxometalates and lanthanide cations or lanthanide-organic complexes. *Inorg. Chem.* **2010**, *49*, 11403.
(35) Naruke, H.; Yamase, T. A novel-type mixed-ligand polyoxotungsto- lanthanoate, $[Ln(BW_{11}O_{39})(W_5O_{18})]^{12-}$ (Ln = Ce^{3+} and Eu^{3+}). *Bull. Chem. Soc. Jpn.* **2000**, *73*, 375.
(36) Armelao, L.; Quici, S.; Barigelletti, F.; Accorsi, G.; Bottaro, G.; Cavazzini, M.; Tondello, E. Design of luminescent lanthanide complexes: From molecules to highly efficient photo-emitting materials. *Coord. Chem. Rev.* **2010**, *254*, 487.
(37) Bünzli, J. C. G.; Piguet, C. Taking advantage of luminescent lanthanide ions. *Chem. Soc. Rev.* **2005**, *34*, 1048.
(38) Zhao, Y.; Yang, X. G.; Lu, X. M.; Yang, C. D.; Fan, N. N.; Yang, Z. T.; Wang, L. Y.; Ma, L. F. $\{Zn_6\}$ Cluster based metal−organic framework with enhanced room-temperature phosphorescence and optoelectronic performances. *Inorg. Chem.* **2019**, *58*, 6215.
(39) Álvarez, E.; Zayas, M. E.; Alvarado-Rivera, J.; Félix-Domínguez, F.; Duarte-Zamorano, R. P.; Caldiño, U. New reddish-orange and greenish-yellow light emitting phosphors: Eu^{3+} and Tb^{3+}/Eu^{3+} in sodium germanate glass. *J. Lumin.* **2014**, *153*, 198.
(40) Zhao, J. W.; Cao, J.; Li, Y. Z.; Zhang, J.; Chen, L. J. First tungstoantimonate-based transition-metal−lanthanide heterometallic hybrids functionalized by amino acid ligands. *Cryst. Growth Des.* **2014**, *14*, 6217.
(41) Zhao, J. W.; Li, Y. Z.; Chen, L. J.; Yang, G. Y. Research progress on polyoxometalate-based transition-metal−rare-earth heterometallic derived materials: synthetic strategies, structural overview and functional applications. *Chem. Commun.* **2016**, *52*, 4418.
(42) Zhang, T.; Spitz, C.; Antonietti, M.; Faul, C. F. J. Highly photoluminescent polyoxometaloeuropate-surfactant complexes by ionic self-assembly. *Chem. - Eur. J.* **2005**, *11*, 1001.
(43) Han, Q.; Wen, Y.; Liu, J. C.; Zhang, W.; Chen, L. J.; Zhao, J. W. Rare- earth-incorporated tellurotungstate hybrids functionalized by 2-picolinic acid ligands: syntheses, structures, and properties. *Inorg. Chem.* **2017**, *56*, 13228.
(44) Chen, Y. H.; Sun, L. H.; Chang, S. Z.; Chen, L. J.; Zhao, J. W. Synergistic effect between different coordination geometries of lanthanides and various coordination modes of 2-picolinic acid ligands tuning three types of rare 3d−4f heterometallic tungstoantimonates. *Inorg. Chem.* **2018**, *57*, 15079.
(45) Liu, J. L.; Jin, M. T.; Chen, L. J.; Zhao, J. W. First dimethyltin-functionalized rare-earth incorporated tellurotungstates consisting of $\{B\text{-}\alpha\text{-}TeW_7O_{28}\}$ and $\{W_5O_{18}\}$ mixed building units. *Inorg. Chem.* **2018**, *57*, 12509.
(46) Chen, L. J.; Zhang, F.; Ma, X.; Luo, J.; Zhao, J. W. Two types of novel tetra-iron substituted sandwich-type arsenotungastates with supporting lanthanide pendants. *Dalton Trans.* **2015**, *44*, 12598.
(47) Liu, Y. J.; Li, H. L.; Lu, C. T.; Gong, P. J.; Ma, X. Y.; Chen, L. J.; Zhao, J. W. Organocounterions-assisted and pH-controlled self-assembly of five nanoscale high-nuclear lanthanide substituted heteropolytungstates. *Cryst. Growth Des.* **2017**, *17*, 3917.
(48) Wu, H. C.; Yan, B.; Li, H. F.; Singh, V.; Ma, P. T.; Niu, J. Y.; Wang, J. P. Enhanced photostability luminescent properties of Er^{3+}-doped near-white- emitting $Dy_xEr_{(1-x)}$-POM derivatives. *Inorg. Chem.* **2018**, *57*, 7665.
(49) Mialane, P.; Lisnard, L.; Mallard, A.; Marrot, J.; Antic-Fidancev, E.; Aschehoug, P.; Vivien, D.; Sécheresse, F. Solid-state and solution studies of $\{Ln_n(SiW_{11}O_{39})\}$ polyoxoanions: an example of building block condensation dependent on the nature of the rare earth. *Inorg. Chem.* **2003**, *42*, 2102.
(50) Rajesh, D.; Dhamodhara Naidu, M.; Ratnakaram, Y. C.; Balakrishna, A. Ho^{3+}-doped strontium−aluminium−bismuth−borate glasses for green light emission. *Luminescence* **2014**, *29*, 854.

DOI: 10.1021/acs.cgd.9b01290
Cryst. Growth Des. 2020, 20, 362−369